Coupling mesoscale transport to catalytic surface reactions in a hybrid model

Fan, Rong; Habibi, Parsa; Padding, Johan T.; Hartkamp, Remco

DOI
10.1063/5.0081829

Publication date
2022

Document Version
Final published version

Published in
Journal of Chemical Physics

The Journal of Chemical Physics

Coupling mesoscale transport to catalytic surface reactions in a hybrid model

Cite as: J. Chem. Phys. **156**, 084105 (2022); https://doi.org/10.1063/5.0081829
Submitted: 10 December 2021 • Accepted: 01 February 2022 • Accepted Manuscript Online: 04 February 2022 • Published Online: 22 February 2022

Rong Fan, Parsa Habibi, Johan T. Padding, et al.

The Journal of Chemical Physics ARTICLE scitation.org/journal/jcp

Coupling mesoscale transport to catalytic surface reactions in a hybrid model

Cite as: J. Chem. Phys. 156, 084105 (2022); doi: 10.1063/5.0081829
Submitted: 10 December 2021 • Accepted: 1 February 2022 •
Published Online: 22 February 2022

Rong Fan,[a] Parsa Habibi,[b] Johan T. Padding,[c] and Remco Hartkamp[d]

AFFILIATIONS

Complex Fluid Processing, Process and Energy Department, Delft University of Technology, Leeghwaterstraat 39, 2628 CB Delft, The Netherlands

Note: This paper is part of the JCP Special Topic on Fluids Meets Solids.
[a]**Electronic mail:** r.fan@tudelft.nl
[b]**Electronic mail:** p.habibi@tudelft.nl
[c]**Electronic mail:** j.t.padding@tudelft.nl
[d]**Author to whom correspondence should be addressed:** r.m.hartkamp@tudelft.nl

ABSTRACT

In heterogeneous catalysis, reactivity and selectivity are not only influenced by chemical processes occurring on catalytic surfaces but also by physical transport phenomena in the bulk fluid and fluid near the reactive surfaces. Because these processes take place at a large range of time and length scales, it is a challenge to model catalytic reactors, especially when dealing with complex surface reactions that cannot be reduced to simple mean-field boundary conditions. As a particle-based mesoscale method, Stochastic Rotation Dynamics (SRD) is well suited for studying problems that include both microscale effects on surfaces and transport phenomena in fluids. In this work, we demonstrate how to simulate heterogeneous catalytic reactors by coupling an SRD fluid with a catalytic surface on which complex surface reactions are explicitly modeled. We provide a theoretical background for modeling different stages of heterogeneous surface reactions. After validating the simulation method for surface reactions with mean-field assumptions, we apply the method to non-mean-field reactions in which surface species interact with each other through a Monte Carlo scheme, leading to island formation on the catalytic surface. We show the potential of the method by simulating a more complex three-step reaction mechanism with reactant dissociation.

I. INTRODUCTION

Heterogeneous catalysis has played an important role in industrial production of chemicals and fuels for over a 100 years.[1] In most industrial applications, heterogeneous catalysts are solids or a mixture of solids, such as metals, transition metal oxides, zeolites, alumina, higher-order oxides, and graphitic carbon. Reactions occur on the active sites on the catalyst surface, which can bind with the reactant molecules. The dispersed catalysts are usually supported by porous materials. The porous support does not only provide a large surface area but can also influence the reaction rates, the conversion, the diffusivities of components, and the lifetime of catalyst.[2–4] Moreover, defects on the surface of the catalyst material have important influence on catalytic activities. This attracts frequent attention from researchers. Defects are caused by various factors in the process of catalyst preparation and can be randomly distributed on the catalyst surface. Due to these features of heterogeneous catalysts, the chemical industry often has to face uncontrolled local catalytic reactions. This results in a series of problems, for example, the formation of hotspots, undesired products, and deactivation of catalysts.

To understand these effects, there is a great need to model the interplay between mass transport rates of reactants and products, adsorption rates of reactants to catalytic surfaces, the rates of different surface reactions, which are possibly influenced by the distribution of reaction intermediates and defects, and desorption rates of the products. This interplay determines the overall reaction rate and selectivity toward a desired product. It also makes the modeling of heterogeneous catalysts a challenging multiscale and multiphysics problem.

A number of computational methods have been used to predict mass transport of reactants and products in heterogeneous catalysis. At the macroscale, direct numerical simulations (DNSs), which model interactions between moving catalyst pellet particles and resolve the fluid flow around them, have many applications for

fluidized bed and packed bed reactors.[5–7] Similarly, discrete element methods (DEMs) can be used if correlations are known for the effective mass transfer rates between the unresolved fluid and catalyst pellet particles.[8–11] Both DNS and DEM methods usually treat the transport of reactants and products inside the pellets through continuum (partial differential) equations for effective pore diffusion. In some cases, partial differential equations are also used on the level of pore networks.[12,13] A disadvantage of such continuum methods is that, although they may describe the macroscale mass transport well, coupling between the continuous concentration fields and catalytic surfaces is typically achieved through source and sink terms (if pores are unresolved) or at best through simplified boundary conditions (if pore surfaces are resolved), for instance, based on Langmuir adsorption kinetics and first-order reactions. With such a continuum approach, it is difficult to properly include microscale finite size (Knudsen and thermal fluctuation) effects.[14] Moreover, it is practically impossible to include changes in reaction rates due to microscale interactions between the different adsorbed species *on* the catalytic surface.

Particle-based methods are better suited to include such microscale effects. In previous studies, reactive systems have been modeled using direct simulation Monte Carlo (DSMC),[15,16] the Lattice-Boltzmann (LB) method,[17–20] and dissipative particle dynamics (DPD).[21,22] Many applications with chemical reactions are simulated with the LB method. However, LB is a pre-averaged method, which does not exhibit the thermal fluctuations without modifications. In this work, we will focus on stochastic rotation dynamics (SRD),[23] a widely used version of multi-particle collision dynamics (MPCD or MPC) methods. SRD provides particular convenience for studying chemical kinetics on reactive surfaces in contact with a thermal bulk fluid through which reactants and products are transported. In SRD, the transport properties are well-defined for arbitrary values of the simulation parameters. Most transport properties are derived analytically. This sets it apart from other particle-based methods such as molecular dynamics and DPD.

Most implementations of chemical reactions in SRD are homogeneous reactions[24,25] or surface reactions with neglect of some processes such as adsorption, surface diffusion, or desorption through the use of mean-field rate expressions.[26,27] Models of colloidal particles propelled by chemical reactions with adsorption–desorption kinetics such as diffusiophoretic Janus colloids and bi-particle catalytic reactions have been described before.[28–33] However, these works do not describe the detailed kinetics of changing catalyst sites. Sengar *et al.* were the first to incorporate a Langmuir–Hinshelwood reaction kinetics by introducing individual steps such as adsorption, desorption, and surface reactions for a pseudo-reaction A → B.[34,35] It has been shown that SRD can simulate heterogeneously catalyzed systems and interlink surface and bulk phenomena, which can occur at different time scales. In addition, the influence of the porous catalyst structure has also been investigated through this method.[36] For realistic catalytic reactions, more complex mechanisms exist, such as multiple elementary reaction steps or "island formation" caused by interactions of surface particles, which lead to deviations from mean-field predictions.[37,38]

In this work, we show for the first time how to model more complex heterogeneous catalytic reactions by coupling an SRD fluid to a catalytic surface on which surface reactions are explicitly modeled. This paper is arranged as follows: In Sec. II, we provide a theoretical background of SRD for modeling hydrodynamics and heterogeneous surface reactions with different mechanisms, including adsorption, particle interaction, and desorption. In Sec. III, we validate the simulation method for different cases of surface reactions with mean-field assumptions and for the surface interactions of species when the mean-field assumptions break. Then, a three-step reaction mechanism with reactant dissociation after adsorption is investigated to demonstrate the capability of the method when simulating more complex reaction mechanisms where mean-field assumptions fail. Finally, in Sec. IV, we give our conclusions and outlook.

II. METHOD

A. Fluid model and simulation setup

In MPC, coarse-grained particles are used to represent the fluid, which evolve in discrete time steps, alternating between particle position updates and momentum exchange. The collisions between multiple particles are accounted for simultaneously rather than treating individual binary collisions of pairs of particles. This makes it computationally more efficient than DSMC when applied to dense fluids. Stochastic rotation dynamics is a widely used version of MPC in which the momentum exchanges via a rotation of the particle relative velocities around a randomly oriented axis.[39]

The hydrodynamics resulting from the SRD method shows Navier–Stokes behavior on large length scales while also automatically accounting for thermal fluctuations and (coarse-grained) molecular diffusion.[40,41] In this technique, the positions and velocities of ideal particles obeying Newton's laws of motion are tracked through time. There are two essential steps. In the streaming step, the position of every particle is advanced in time using its respective velocities by an Euler scheme. Then, in the collision step, a grid divides the volume into cubic cells. The grid is shifted randomly before every collision step to ensure Galilean invariance,[42] and "ghost particles" are added in cells overlapping with walls to correct the fluid viscosity and velocity there. Afterward, the particle velocities relative to the center of mass velocity in each cell are instantaneously rotated by a given angle around a randomly chosen axis to mimic the exchange of fluid momentum. To increase the accuracy of handling wall collisions, multiple streaming steps per collision step can be taken, i.e., the collision time interval can be an integer multiple of the streaming integration time step.

Figure 1 shows the simulation setup. In this geometry, the top and bottom surfaces are solid and the sides of the domain are periodic. The bottom wall is reactive (the boundary condition depends on the reaction that is simulated), while the top wall has a no-flux boundary with respect to concentration (inert wall). An adjusted stochastic boundary condition[43,44] is applied on the reactive surface in order to account for particle adsorption/desorption. In this work, these events happen during the streaming step. Particles colliding with the wall have a probability of adsorbing. Once adsorbed, the particle remains adsorbed, reacts, or desorbs based on a probability. The reactive wall is divided into lattice grids. Each grid represents a catalyst site, which is occupied when a particle is absorbed.

The choice of basic units is shown in Table I. The choice of simulation parameters in this work is streaming time interval (Δt_s) as 0.1, collision time interval (Δt_c) as 1, collision angle (α) as $\pi/2$, and

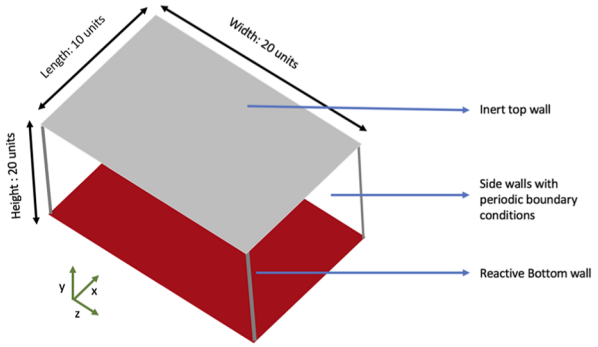

FIG. 1. Schematic of the simulation setup. Periodic boundary conditions are employed for the sides while the top (inert) and bottom (reactive) surfaces are solid walls.

TABLE I. Simulation parameters of SRD and derived units. In our simulations, the collision cell size, majority species mass, and thermal energy at the reference temperature are the units of length, mass, and energy, respectively.

SRD fluid simulation parameters	
$a_0 \equiv 1$	Collision cell size
$m_0 \equiv 1$	Solvent (majority species) mass
$k_B T_0 \equiv 1$	Thermal energy (at reference temperature)
γ	Average number of particles per collision cell
Δt_s	Streaming integration time step
Δt_c	Collision time interval
α	SRD rotation angle
Derived units	
Density	m_0/a_0^3
Time	$t_0 = a_0\sqrt{\frac{m_0}{k_b T_0}}$
Diffusion coefficient	$D_0 = \frac{a_0^2}{t_0} = a_0\sqrt{\frac{k_b T_0}{m_0}}$

average particle density per cell (γ) as 25. This high particle density is chosen in consideration of obtaining smooth concentration profiles.

The transport properties of the SRD fluid can be analytically expressed in terms of simulation parameters such as the collision time step (Δt_c), the number density of particles (γ), the thermal energy $k_b T$, the cell size (a_0), and the mass of the particle (m_i). The fact that these analytical expressions, shown in Table II, exist simplifies the use of SRD and reduces the need for trial and error simulations. The analytical expression for the (kinematic) shear viscosity ν has been derived and validated by Ihle and Tüzel.[45–47] Unlike the shear viscosity, no analytical expression for the collisional contribution to the self-diffusion coefficient has been derived due to the difficulty of theoretically including effects of hydrodynamic correlations on the self-diffusivity.[39,48] The expression for the collisional contribution is derived from the assumption of molecular chaos. Therefore, the expression for the self-diffusion coefficient is most

TABLE II. Kinetic (streaming) and collisional contributions to SRD transport coefficients for a three-dimensional single-component SRD fluid, valid up to the order $1/\gamma^2$. Note that the shear viscosity is expressed as a kinematic viscosity, i.e., with the same units as self-diffusivity.

Kinetic contribution $\times k_B T \Delta t_c/(2m)$
Shear viscosity $\nu = \frac{5\gamma}{(\gamma-1+e^{-\gamma})[2-\cos\ \alpha-\cos(2\alpha)]} - 1$
Self-diffusivity $D_s = \frac{3\gamma}{(\gamma-1+e^{-\gamma})(1-\cos\ \alpha)} - 1$
Collisional contribution $\times\ a_0^2/\Delta t_c$
Shear viscosity $\nu = \frac{1}{18\gamma}(\gamma - 1 + e^{-\gamma})[1 - \cos\ \alpha]$

accurate when the dimensionless mean free path ($\lambda = \Delta t_c/t_0$) is larger than 0.6.[49]

In SRD, the temperature is not set as a direct parameter but is inherent in the particles' velocity fluctuations. The temperature can be controlled by modulating the velocity fluctuations, which can be done through various thermostatting schemes. For example, the Andersen thermostat reassigns the fluctuating velocities in each time step stochastically based on the Maxwell–Boltzmann distribution,[23] and the Nosé–Hoover thermostat couples the system with an external reservoir in a way that allows for fluctuations in temperature.[50,51] In this work, a direct temperature scaling is used to maintain a strictly isothermal system: in the collision step, we add for each cell c containing $n_c \geq 2$ SRD particles the kinetic energy associated with velocity fluctuations, $K = \sum_{cell\ c}\sum_i^{n_c} \frac{1}{2} m_i \delta v_i^2$, and the number of degrees of freedom, $n_{free} = \sum_{cell c} 3(n_c - 1)$. This allows us to calculate an instantaneous global temperature $k_B T_{current} = 2K/n_{free}$ based on the velocity fluctuations in the entire system, independent of any convective flow velocities. Subsequently, the relative velocities in each cell are scaled by a factor $\sqrt{T_{target}/T_{current}}$, where T_{target} is the target temperature. This "strong coupling" scheme is simple to apply and, however, does not allow for fluctuations in the instantaneous global temperature. Such a simplification is only justified if one is dealing with a very large number of particles for which statistical mechanics predicts that the relative fluctuations in total energy ($\delta K/K \propto 1/\sqrt{n_{free}}$) are very small.

When dealing with multi-component mixtures, frictional forces between different components may lead to some unexpected behavior that cannot be explained by Fickian diffusion. A Maxwell–Stefan diffusion model is employed instead. In this framework, the driving force of transport, which is linked to the spatial derivative of the chemical potential, can be balanced with the frictional forces. In SRD, multi-component diffusion is imposed due to the collision step that treats molecules based on their particle mass. The particle velocities are adjusted based on the center of the mass velocity (mass weighted average velocity). For this reason, molecules with a large mass undergo smaller changes in velocity in the collision step than a particle with a smaller mass.[39] The Maxwell–Stefan diffusion coefficients $-\mathrm{D}_{ij}$ cannot be calculated *a priori*, but they can be estimated. In binary dilute mixtures, the Darken equation can be used,

$$Đ_{12} = x_1 D_{2s} + (1 - x_1) D_{1s}, \tag{1}$$

where D_{1s} and x_1 represent the self-diffusivity and mole fraction of species 1, respectively. This relation is used later when dealing with mixtures containing particles with varying masses.

B. Reaction scheme

A typical heterogeneous reaction involves the adsorption of the reactant on the catalyst surface, breaking of one or more chemical bonds, formation of new bonds, and finally the desorption of the product. Owing to the coarse-grained nature of mesoscopic simulations, heterogeneous chemical reactions can be simplified using random adsorption and desorption events and reactions in steps, as explained in the following.

1. Adsorption, reaction, and desorption

In this hybrid model, adsorption, reaction, and desorption are taken into account explicitly and updated every streaming time step (Δt_s). The implementation of the adsorption and desorption method is discussed in detail in our previous work.[44] When a particle collides with the wall, the adsorption site closest to the collision point is checked; if this site is vacant, the particle may adsorb with probability P_{ads}. Every Δt_s, the adsorbed particles are also updated for the reaction. For a simple $A \rightarrow B$ reaction, a probability test (with a reaction probability P_{re}) is carried out. If the probability test is successful, A will convert to B. For simple first-order reactions, the reaction rate does not depend on the surrounding of the particle. However, bi-particle elementary particles are treated differently for mean-field and non-mean-field reactions. For a mean-field $A + B \rightarrow C$ reaction, for every adsorbed particle A, a random catalyst site is picked on the wall; if the random site is of type B, a reaction may occur with a probability P_{re}. If the reaction occurs, one of the reactants turns to a type C, while the other reactant site becomes vacant. Note that for reactions involving two different species, only one of the adsorbed species is checked for the reaction. In the case of non-mean-field reactions, a particle can only react with its (first and second closest) neighboring particles, and surface diffusion (including possible surface interactions) is modeled explicitly. The details for non-mean-field implementation can be found in Subsection II B 2. For the desorption of the species from the wall, a test with desorption probability P_{des} is carried out. If the probability test is successful, the particle is given a velocity based on a Maxwell–Boltzmann distribution and reintroduced into the bulk. For cases in which there is a bulk flow, the velocity distribution would need to be adjusted to obtain correct flow profiles. The choice for the distributions and their validation is described in detail in our previous work.[44]

To validate the simulation results obtained from SRD, it is necessary to be able to convert probabilities for adsorption, reaction, and desorption into rate constants that can be used in continuum numerical models. To relate the adsorption rate constant to simulation parameters, first, a relation needs to be found for the particle collision frequency (Z) with the adsorbing wall,

$$Z = \frac{1}{2}\frac{N}{V}\langle|v_y|\rangle. \tag{2}$$

As shown in Eq. (2), the collision frequency can be expressed in terms of the particle concentration ($C_s = N/V$) and the average velocity in the y-direction, which is perpendicular to the wall, $\langle|v_y|\rangle = \sqrt{2k_bT/(\pi m)}$.[34]

Not every collision leads to adsorption, and in order to calculate the rate of particle adsorption R_{ads}, the adsorption probability P_{ads} and the fraction of unoccupied catalyst sites θ_v need to be considered. Therefore, based on SRD parameters, the rate of adsorption can be expressed as

$$R_{ads} = P_{ads}Z\theta_v = C_sP_{ads}\theta_v\sqrt{\frac{k_bT}{2\pi m}}. \tag{3}$$

The rate of adsorption can also be calculated using a mean-field expression involving the adsorption rate constant (k_{ads}),

$$R_{ads} = k_{ads}C_s\theta_v\frac{N_{cat}}{A_{cat}}, \tag{4}$$

where A_{cat} represents the catalytic surface area and N_{cat} is the number of catalyst sites. An expression for k_{ads} can be obtained by combining Eqs. (3) and (4),

$$k_{ads} = \sqrt{\frac{k_bT}{2\pi m}}\frac{P_{ads}A_{cat}}{N_{cat}}. \tag{5}$$

A similar approach can be used to relate the desorption and first-order reaction rate constants to simulation parameters. Given an example of a first-order reaction A → B, the rate constant is given by

$$k_{re} = \frac{\ln(1 - P_{re})}{\Delta t_s} \tag{6}$$

in which P_{re} represents the probability for the reaction. Analogously, the desorption rate constant of product particle B can be expressed as

$$k_{des} = \frac{\ln(1 - P_{des})}{\Delta t_s}, \tag{7}$$

where P_{des} is the probability for the desorption of a B particle in a time interval Δt_s.

2. Surface interactions

The reaction expression with mean-field assumption has been derived in Sec. II B 1. Here, we discuss the case in which the mean-field assumption breaks down.

The mean-field approximation is a commonly made assumption to turn a many-body problem into a single-body problem[51] and to reduce the complexity and computational cost of solving a system. However, the mean-field assumption is not always reasonable, for it is limited to cases in which no inter-species interactions exist and where the rate of surface diffusion is large such that all species instantaneously adopt an even distribution over the surface. To simulate surface interactions of particles and their possible separation into "islands" of different species, we use mesoscopic Monte Carlo simulation. Interactions between neighboring adsorbed particles are accounted for in an explicit manner by changes in the potential energy of the adsorbed particles.[52] To fit the Monte Carlo step in SRD time steps, surface mobilities are assumed to be large enough to maintain a local equilibrium on the surface.

The catalytic surface is divided into a surface lattice grid. The size, shape, and orientation of this surface lattice grid can be chosen depending on the specific problem at hand, independently of the size and orientation of the cubic SRD grid. For convenience, in the simulations presented here, the catalytic surface is divided into a square lattice aligned with the SRD grid in which each particle can interact with its first and second nearest neighbors. The division of the surface into a square grid leads to fixed catalyst sites. Although this simplified setting does not allow for the occurrence of complex kinetics such as surface reconstruction, it can be extended to study a variety of reactions in which surface interactions are prevalent. An example includes the adsorption and dissociation of oxygen in Pt(111), which is influenced by nearby chemisorbed species.[53–56] The main focus of this work is to give an example of coupling the fluid phase to the surface reaction phenomena by implementation of non-mean-field effects in SRD, something which is not available with most kinetic Monte Carlo simulations. The distance between two neighboring surface sites is set to $b_0 = a_0/4$ with a_0 corresponding to one SRD cell such that there are 16 catalyst sites per a_0^2. In this mesoscopic Monte Carlo simulation, a similar procedure as the metropolis algorithm is used. The Monte Carlo steps occur five times per each adsorbed particle every streaming time step (Δt_s). In each Monte Carlo step, a random particle may move to one of its four closest neighboring lattice cells, provided that it meets certain requirements. A move is directly accepted if the particle in the new position leads to a lower potential energy. Otherwise, the move may still be accepted with a probability of $P_{acc} = \exp(-(E_{after} - E_{before})/(k_B T))$. To implement this, a uniform random number between 0 and 1 is picked and the move is accepted if this number is lower than P_{acc}. If only repulsive interactions between different species are considered, then, the following expression can be used to calculate the total energy:

$$E = \frac{E_0}{2}\sum_{i=1}^{N_{ads}}\sum_{j\in Z_{i,1}}(1-\delta(s_i - s_j)) + \frac{E_1}{2}\sum_{i=1}^{N_{ads}}\sum_{j\in Z_{i,2}}(1-\delta(s_i - s_j)). \quad (8)$$

In this expression, E_0 and E_1 are the first and second nearest neighbor repulsive pair interactions between two adsorbed particles of different species. N_{ads} is the total number of particles adsorbed on the wall while $Z_{i,1}$ and $Z_{i,2}$ refer to the first and second neighbor list for particle i. $\delta(s_i - s_j)$ is the Dirac delta function, which is equal to 1 when the types of the species on the wall (denoted with s_i and s_j) are equal to each other and 0 otherwise. Another condition that is placed on the particle movement is that it can only enter a new site if that site is unoccupied. This mimics the fact that particle movement becomes limited when the catalyst sites are nearly all occupied.

The choice of which neighbor interactions to account for when calculating the potential energy can be important in determining the shape of the boundaries formed between two different species on the surface. Square lattices, taking into account only the four nearest neighbors, lead to the formation of square boundaries, which do not adequately represent the shape of most real phase-separated domains. As shown in Fig. 2, if inter-species interactions are assumed to be unfavorable (positive energetic contribution), then, by only counting the nearest neighbor interactions, the energy

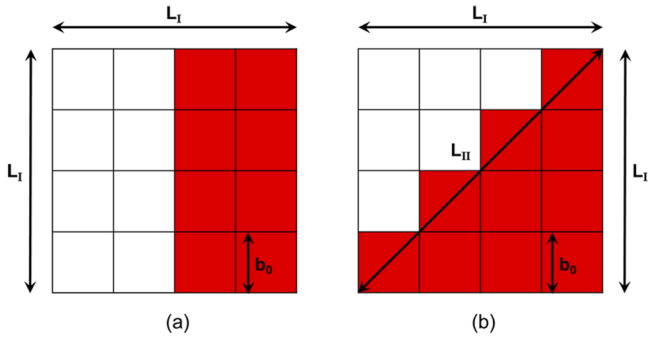

FIG. 2. Straight (a) and slanted (b) boundaries that can form between two different species. "b_0" refers to the unit square lattice size and L_I is the boundary length (between the red and white species) of configuration I and is equal to the side length of the square lattice. L_{II} is equal to the boundary length of configuration II.

(E_I) of a straight line boundary (configuration I) per boundary length (L_I) is equal to $\frac{E_I}{L_I} = \frac{E_0}{b_0}$. In this expression, E_0 refers to the nearest neighbor inter-species interaction and b_0 is the square lattice unit size. Meanwhile, the energy for configuration 2/unit length of the boundary is given by $\frac{E_{II}}{L_{II}} = \frac{2E_0}{\sqrt{2}b_0} = \frac{\sqrt{2}E_0}{b_0}$. To enable more isotropic growth of the boundaries, both configuration I and II need to become equally favorable. This can be achieved by also taking into account the second nearest neighbor interactions (denoted by E_1).[52] In that case, the energy of configuration I and II per unit length of the boundaries can be expressed by

$$\frac{E_I}{L_I} = \frac{E_0 + 2E_1}{b_0}, \quad (9)$$

$$\frac{E_{II}}{L_{II}} = \frac{2E_0 + E_1}{\sqrt{2}b_0}. \quad (10)$$

The two expressions (energy per unit length) are equal if the following ratio is chosen between E_1 and E_0:

$$\frac{E_1}{E_0} = \frac{\sqrt{2}-1}{2-\sqrt{2}} = \frac{1}{\sqrt{2}}. \quad (11)$$

III. VALIDATION AND RESULTS

In our previous work,[44] we validated the adjusted stochastic boundary condition leading to thermostatting walls with a very small slip velocity in the case of convective flow. Since the present work focuses on simulating surface reactions with SRD, here, we validate the method for Langmuir kinetic reactions and more complex reactions in a reactor without flow.

A. First-order surface reaction

In this section, a simple Langmuir kinetic model will be investigated. In the simulation, a particle of type A can adsorb on the wall with a probability $P_{ads} = 0.20$ (corresponding to $k_{ads} = 0.08 a_0^3 t_0^{-1}$) and can also react to become type B ($P_{re} = 0.01$, leading to $k_{re} = 0.1 t_0^{-1}$) and desorb ($P_{des} = 0.01$, leading to $k_{des} = 0.1 t_0^{-1}$). Species B

can also adsorb and desorb from the wall with the same probabilities as species A. The reaction kinetics is expressed by

$$A + * \rightleftharpoons A* \longrightarrow B* \rightleftharpoons B + *, \tag{12}$$

where * refers to a vacant site on the surface and A^* refers to a surface site on the wall occupied by species A (the same nomenclature applies to species B and B^*). This simulation allows for the validation of the adsorption–reaction–desorption implementation in the SRD code. In terms of mean-field equations, the rate of change in surface coverage of A and B can be expressed as

$$\frac{d\theta_A}{dt} = k_{ads,A}\theta_V \gamma(t) x_A(y=0,t) - k_{re}\theta_A - k_{des,A}\theta_A, \tag{13}$$

$$\frac{d\theta_B}{dt} = k_{ads,B}\theta_V \gamma(t) x_B(y=0,t) + k_{re}\theta_A - k_{des,B}\theta_B, \tag{14}$$

where $x_A(y=0,t)$ is the local mole fraction of species A in the fluid near the catalytic surface located at $y=0$ and $\gamma(t)$ is the number density of particles in the fluid. θ_A, θ_B, and θ_V are the surface coverage of particle A, B, and vacant sites, respectively. The adsorption rate depends on the collision frequency of particle A, which is influenced by the mole fraction of A $[x_A(y=0,t)]$ in the fluid and the number density $\gamma(t)$ of particles in the fluid. When the simulation starts $(t=0)$, at the surface, the initial condition of the fraction of particle A, B, and vacant site is $\theta_A = 0, \theta_B = 0, \theta_V = 1$. A continuum numerical model is used to validate the simulation by solving the unsteady diffusion equation for each species i in the fluid,

$$\frac{dC_i}{dt} = D_i \frac{d^2 C_i}{dy^2} \tag{15}$$

with boundary conditions taking into account the rates of adsorption and desorption as shown in Eq. (A3) in Appendix A. Here, C_i represents the concentration of species i in the fluid, which can be obtained by multiplying the particle number density $\gamma(t)$ by the local mole fraction x_i, and D_i represents the diffusion coefficient of species i. In the numerical code, $\gamma(t)$ is assumed to be independent of local variations and the number of particles that adsorb to or desorb from the surface (or are reduced/added due to the reaction) and are spread homogeneously over the SRD cell. This assumption is justified by the low adsorption probabilities that are used (all below 0.20) coupled with the large number of particles (100 000 particles in total) with respect to the number of catalyst sites (3200). For large adsorption/desorption probabilities and low particle number densities, the local variations of local particle number densities may lead to advection effects. SRD may be capable of including these effects; however, the study of these systems is beyond the scope of this work and is encouraged for further research. In the numerical model, the governing equation Eq. (15) is discretized using a finite volume scheme. The details of the numerical model are given in Appendix A.

The numerical and simulation results for the concentration profile after $10t_0$ are depicted in Fig. 3(a) along with the vacancy fraction as a function of time in Fig. 3(b). An excellent agreement is observed between the SRD simulation results for both the concentration profile in the bulk and for the vacancy fraction at the wall. Only small reaction rates are considered in this section to ensure that the concentration gradients near the reactive wall are small. Large concentration gradients will require a more elaborate expression for the mean-field adsorption rate constant, which is beyond the scope of this work (see Appendix A for more explanation on the numerical scheme for validation).

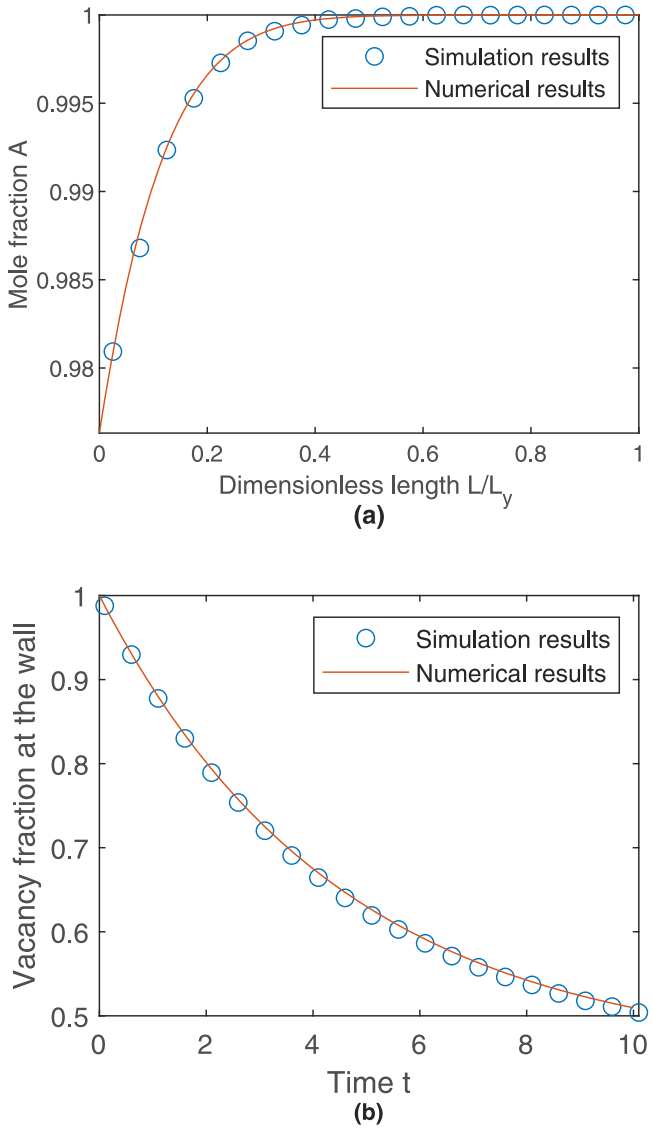

FIG. 3. First-order mean-field surface reaction. (a) Concentration profile at a cross section of an infinite channel. (b) Vacancy fraction on the reactive wall shown as a function of time.

B. Bi-particle reactions

Before simulating complex reaction mechanisms, it is necessary to be able to simulate bi-particle elementary reaction steps on the catalytic surface. In this section, bi-particle reactions $A + B \rightarrow C$ and $A + * \leftrightarrow 2B$ are simulated under the mean-field assumption and validated using numerical models. In order to use numerical validations,

the rate constant of bi-particle reactions needs to be expressed in terms of simulation parameters (such as the probability of the reaction). This calculation is done for a $A + B \rightarrow C$ reaction as a test case, but the results can be generalized for other bi-particle reactions.

Assuming that at a given time step there is no adsorption/desorption occurring concurrently, the rate of change in the number of catalyst sites occupied by species A and B over time can be described by Eqs. (16) and (17) using the mean-field assumption,

$$\frac{d\rho_{S,A_i}}{dt} = -k_{r,AB}\rho_{S,A_i}\rho_{S,B_i}, \tag{16}$$

$$\frac{d\rho_{S,B_i}}{dt} = -k_{r,AB}\rho_{S,A_i}\rho_{S,B_i}. \tag{17}$$

In these expressions, ρ_{S,A_i}, ρ_{S,B_i}, and $k_{r,AB}$ refer to the total number of sites occupied per area of the catalyst by species A and B and the reaction rate constant in the mean-field model, respectively. A Taylor series expansion can be made to find an approximate expression for ρ_{S,A_i} and ρ_{S,B_i}, calculated with their number density in the previous time step ($\rho_{S,A_{i-1}}$, $\rho_{S,B_{i-1}}$),

$$\rho_{S,A_i} \approx \rho_{S,A_{i-1}} + \frac{d\rho_{S,A_i}}{dt}\Delta t_s, \tag{18}$$

$$\frac{\rho_{S,A_i}}{\rho_{S,A_{i-1}}} \approx 1 - k_{r,AB}\rho_{S,B_{i-1}}\Delta t_s. \tag{19}$$

In terms of simulation parameters and given the implementation of the bi-molecular surface reactions, the fraction $\frac{\rho_{S,A_i}}{\rho_{S,A_{i-1}}}$ can be expressed as

$$\frac{N_A}{N_{A_{i-1}}} = \frac{\rho_{S,A_i}}{\rho_{S,A_{i-1}}} = 1 - P_{re,AB}\theta_{B_{i-1}}, \tag{20}$$

where $P_{re,AB}$ refers to the probability of the reaction and θ_B is the fraction of sites occupied by particle B ($\theta_B = A_{cat}\rho_{S,B}/N_{cat}$). The reaction rate constant of $A + B \rightarrow C$ can be inferred by combining Eqs. (19) and (20) as follows:

$$k_{r,AB} = \frac{A_{cat}P_{re,AB}}{N_{cat}\Delta t_s}. \tag{21}$$

The expression of maximum error (Er) associated with Eq. (19) can be calculated from the second derivative of ρ_A with respect to time (see Appendix B). Using this reaction rate constant, the mean-field expressions for the change in the fraction occupied by A, B, and C can be calculated,

$$\frac{d\theta_A}{dt} = k_{ads,A}\theta_V\gamma(t)x_A(y=0,t) - k_{des,A}\theta_A - \frac{k_{r,AB}N_{cat}}{A_{cat}}\theta_A\theta_B, \tag{22}$$

$$\frac{d\theta_B}{dt} = k_{ads,B}\theta_V\gamma(t)x_A(y=0,t) - k_{des,B}\theta_B - \frac{k_{r,AB}N_{cat}}{A_{cat}}\theta_A\theta_B, \tag{23}$$

$$\frac{d\theta_C}{dt} = k_{ads,C}\theta_V\gamma(t)x_A(y=0,t) - k_{des,C}\theta_C + \frac{k_{r,AB}N_{cat}}{A_{cat}}\theta_A\theta_B, \tag{24}$$

where γ and x_A represent the number density of the fluid and the mole fraction of species A in the fluid. At time $t = 0$, the reaction is catalyzed on the wall at $y = 0$. The initial mixture consists of reactants A and B in equal amounts. The masses of A and B particles are set to 1 m_0, and the mass of C is set to 2 m_0. Considering that the mass of the product is different, it implies that it has a different self-diffusion coefficient than the reactants (see Table II). To simplify the validation test case, it is ensured that the production rate is low ($P_{ads,A} = 0.05$ corresponding to $k_{ads,A} = 0.001\,25$ and $P_{des,A} = 0.0001$ corresponding to $k_{des,A} = 0.001$). This implies that the influence of the C species on the diffusivities in the bulk can be ignored for the time scales considered in this simulation. In this validation case, the same probability of desorption and adsorption is used for every species involved. Therefore, in this case, $k_{des,A} = k_{desandB} = k_{des,C}$. As the mass of species C is set as twice that of the reactants, $k_{ads,A} = k_{ads,B} = \sqrt{2}k_{ads,C}$. Equations (22)–(24) are coupled to the numerical equations shown in Appendix A to find the evolution of mole fractions $x_A(y,t)$, $x_B(y,t)$, and $x_C(y,t)$ and the number density $\gamma(t)$. $k_{r,AB}$ is calculated with Eq. (21) derived previously.

The very good agreement between the numerical and simulation results in Fig. 4 confirms the validity of the expression found for $k_{r,AB}$. Consistent with the error expression in Appendix B, the best agreement is found for the lowest reaction probabilities, 0.1 and 0.2. The error for the $k_{r,AB}$ expression is shown in Appendix B to scale with the square of the reaction probability ($P_{re,AB}$). In order to simulate reactions with higher reaction rate constants, it is therefore advised to lower the time step Δt_s. This means that the catalyst sites on the wall are updated more frequently, and thereby, lower reaction probabilities can be used to obtain the same reaction rates.

Another validation test is done with a reversible reaction: $A + * \leftrightarrow 2B$. At the start of the reaction, the solution only contains particles of type A ($x_A = 1$). To conserve mass, the mass of A is set to 2 ($m_A = 2$) and the mass of B is set to 1 ($m_B = 1$). Three different

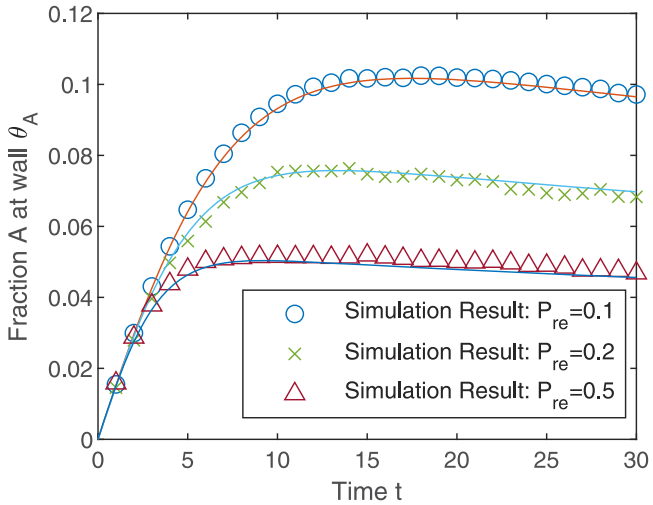

FIG. 4. Simulation results (symbols) and continuum numerical results (lines) for a mean-field bi-particle reaction $A + B \rightarrow C$ for different reaction probabilities (0.1, 0.2, and 0.5).

reaction probabilities of 0.1, 0.2, and 0.5 are used. The same probability of reaction is used for the forward and backward reaction. This would correspond to a $k_{r,A\leftrightarrow 2B}$ of 0.0625, 0.125, and 0.3125, respectively. The same probability of adsorption ($P_{ads} = 0.05$) and desorption ($P_{des} = 0.0001$) was used as in Subsection III A for both species A and B. This corresponds to $k_{des,A} = 0.001$ and $\sqrt{2}k_{ads,A} = k_{ads,B} = 0.001\,25$. The rate of change in the catalyst occupation of A and B (denoted by θ_A and θ_A) is given by

$$\frac{d\theta_A}{dt} = k_{ads,A}\theta_V\gamma(t)x_A(y=0,t) - k_{des,A}\theta_A - \frac{k_{r,A\leftrightarrow B}N_{cat}}{A_{cat}}\theta_A\theta_V + \frac{k_{r,A\leftrightarrow B}N_{cat}}{A_{cat}}\theta_B^2, \tag{25}$$

$$\frac{d\theta_B}{dt} = k_{ads,B}\theta_V\gamma(t)x_B(y=0,t) - k_{des,B}\theta_B + \frac{k_{r,A\leftrightarrow B}N_{cat}}{A_{cat}}\theta_A\theta_V - \frac{k_{r,A\leftrightarrow B}N_{cat}}{A_{cat}}\theta_B^2. \tag{26}$$

The numerical and simulation results are shown in Fig. 5. The reaction shows an initial non-linearity, which ceases at $t > 7$. The onset of this quasi-steady state originates from the reversibility of the reaction. As it proceeds, the production and consumption terms of A and B equilibrate, and mainly, the linear growth due to adsorption is observed. This equilibration of the non-linear reactive terms happens more rapidly when $k_{r,A\leftrightarrow B}$ becomes large compared to the other process rates (desorption and adsorption). At later stages, it is expected that the fraction of A at the wall will equilibrate. This will occur when the vacant surface sites become more occupied, thereby making the adsorption and desorption process reach the same rate. However, this is still not observed at the time scales considered ($0 < t < 10$). Based on Fig. 5, the simulation seems capable in representing both the non-linear change in the initial stage ($t < 5$) and the increase in the latter stage.

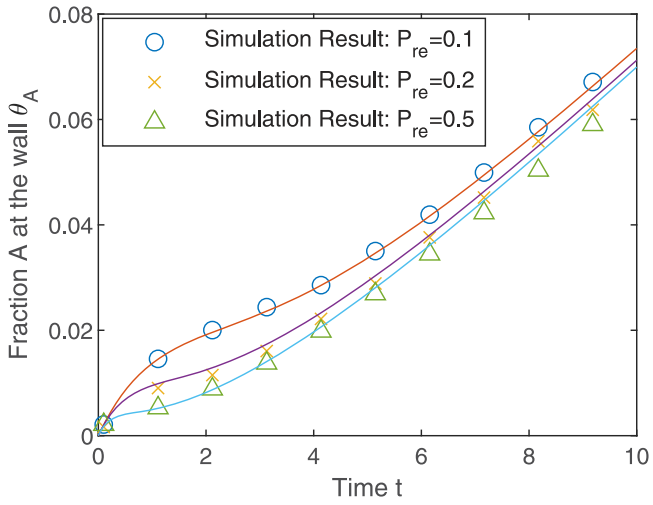

FIG. 5. Simulation results (symbols) and numerical results (lines) for a mean-field reversible reaction $A + * \rightarrow 2B$ for different reaction probabilities (0.1, 0.2, and 0.5).

C. Surface interaction

After having validated the bi-particle mean-field reactions, it is now possible to simulate more complex surface reactions in which the mean-field assumptions are no longer valid. This applies to reactions in which the unfavorable interactions between different adsorbed species lead to species separation and formation of

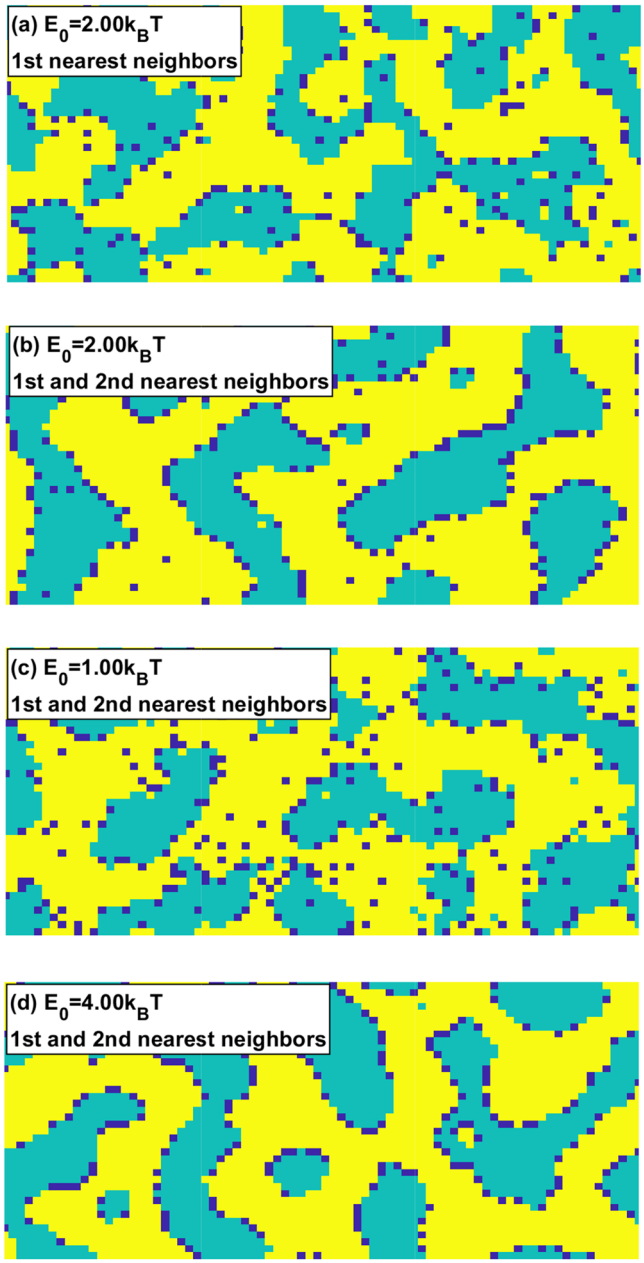

FIG. 6. Island formation between two species A and B with different energetic interaction (E_0) between two adjacent inter-species and taking into account different neighbors. The yellow, green, and blue color represent A, B, and vacant sites, respectively.

"islands." Examples of such reactions include heterogeneously catalyzed nitrogen oxide reduction by ammonia[57] or hydrogen[58] and the CO oxidation reaction.[59] In this section, the influence of island formation on the reaction rate of a $A + B \rightarrow C$ reaction is evaluated by drawing comparisons with mean-field reactions that were discussed previously. The method of simulating the surface interactions of particles and the consequent separation of particles into islands is described in Sec. II.

Figure 6 shows that boundaries are less isotropic when only nearest neighboring interactions are considered than when second neighboring interactions are also included. This finding indicates that the second neighboring interactions should be considered at the very least for a realistic accounting of the surface interactions. Taking additional neighboring interactions into account can lead to more isotropic boundaries but will increase the computational cost.

To demonstrate island formation, only repulsive forces between two separate species are considered in this study. However, separation between the particles can also occur if the interactions of the species with themselves are more favorable than the inter-species interactions. The magnitude and sign of interactions will depend on the species that are simulated. The influence of having different magnitudes of interactions is considered here to demonstrate its consequence for the coupling between the SRD simulation and the mesoscopic Monte Carlo method.

To study the influence of island formation on bi-particle reaction rates, a $A + B \rightarrow C$ reaction is considered. This reaction was also studied in Sec. III B under mean-field conditions at different reaction rates. A probability of the reaction of 0.1 (corresponding to a mean-field rate constant of 1 a_0^2/t_0) is studied. An E_0 of $2.00 k_B T$ is considered (second neighboring interactions are included as described in Sec. II) with five Monte Carlo steps per adsorbed particle at each Δt_s. This corresponds to islands formed on the scale of around 5 a_0 [similar to the islands in Fig. 6(b)].

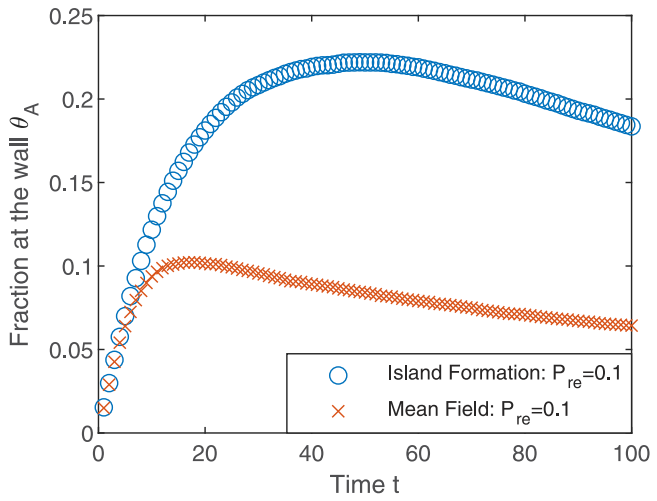

FIG. 7. Influence of island formation on bi-molecular reactions. The same probability of reaction (P_{re} = 0.1) is used for both the mean-field and non-mean-field, island forming model. The initial mixture consists of 50% (molar) of species A and 50% of species B.

Figure 7 shows that surface interactions (i.e., the case of island formation) can have a considerable influence on the reaction rate. As species A and B have unfavorable interactions, the probability that they come into contact is lowered with respect to the mean-field assumption. This lowers the reaction rate. This effect is prominent especially in the initial stages when the reactants A and B can avoid being in contact (as most of the catalyst sites are vacant). From Fig. 7, adsorption is the dominating mechanism up until the time of $t = 30$ after which depletion of A occurs as the reaction rate becomes prominent. The same transition between dominant mechanisms occurs already at $t = 10$ for the mean-field case. Consequently, the maximum fraction of A on the surface is approximately twice as high when island formation is considered. This notable change signifies the importance that surface interactions can have in reaction mechanisms.

D. Elementary reaction

The methods developed so far are applied to simulate a gas-phase reaction involving three different elementary steps to show the potential usage of SRD in the heterogeneously catalyzed reaction. An example of a typical industrially relevant reaction explained in terms of this mechanism is CO oxidation. Since this reaction involves a mixture of components, a multi-component diffusion model is needed to accurately predict the concentration profiles that form in the catalytic channel. For such surface reactions, catalysts are inherently dynamic in nature. Dynamic surface behavior such as surface reconstruction has been investigated in various experimental works and molecular simulations.[60–64] The objective of the current work is to mimic the mechanism, not to incorporate full atomistic details of the surface kinetics for a certain reaction. Effects of surface reconstruction and specific crystal structures are not considered in this work. There is a clear distinction between our test case and a real CO oxidation reaction in the sense that the surface ordering of the species and locations of O(ads) and CO(ads) on the surface would need a more thorough consideration [e.g., to consider short length O(ads)–O(ads) repulsion and surface restructuring that can occur at higher O(ads) fractions].

The simulation considered in this section involves 3 species in the SRD domain, namely, species A, B_2 (the notation B_2 is picked because this species will dissociate into $2B_{ads}$ on the surface), and the product C. Species A has a unit mass m_0, species B_2 is given a mass of 1.17 m_0, and species C is given a mass of 1.57 m_0 to mimic the mass ratio of CO, O_2, and CO_2, respectively. Due to the differences in mass, it can be seen that the species considered have different self-diffusion coefficients (see Table II). Specifically, the self-diffusion coefficient of species A is around 15% higher than that of B_2 and around 36% higher than that of species C. This difference warrants the need for a multi-component diffusion model. Based on the mechanism of CO oxidation, the change in these three species through the surface catalyzed reaction is shown in the following:

$$A + * \leftrightarrow A_{ads}, \tag{27}$$

$$B_2 + 2* \rightarrow 2B_{ads}, \tag{28}$$

$$A_{ads} + B_{ads} \rightarrow C + 2*. \tag{29}$$

In this reaction mechanism, species A and B_2 adsorb on the catalyst surface with an adsorption probability of 0.05, while C does not undergo adsorption. To simulate catalyst poisoning, species A_{ads} is given a low desorption probability of 0.0001, while B_{ads} does not undergo desorption. A_{ads} and B_{ads} have unfavorable repulsive interactions ($E_0 = 2k_bT$) and can react together with a probability of 0.1 to form the product C. Upon formation, C desorbs off the wall instantaneously. To test the mechanism and probe the influence of the initial composition on the reaction rate and the fraction induced on the wall, three different compositions are tested. These compositions consist initially only of reactants at A to B_2 molar ratios of 1:1, 2:1, and 1:2. In Fig. 8(a), the fraction of A_{ads} and B_{ads} on the wall is shown over time for an equimolar initial mixture of A and B_2. This composition is more optimal compared to the other two compositions as none of the species is fully poisoning the catalyst by excessively occupying the catalytic sites. Furthermore, as the fractions of A_{ads} and B_{ads} are both high (at least until time $t = 100t_0$), the largest production rate is expected. The large fractions of A_{ads} and B_{ads} are especially important in this reaction mechanism as island formation of A and B is considered (as the species will tend to avoid each other when the occupied fractions are smaller).

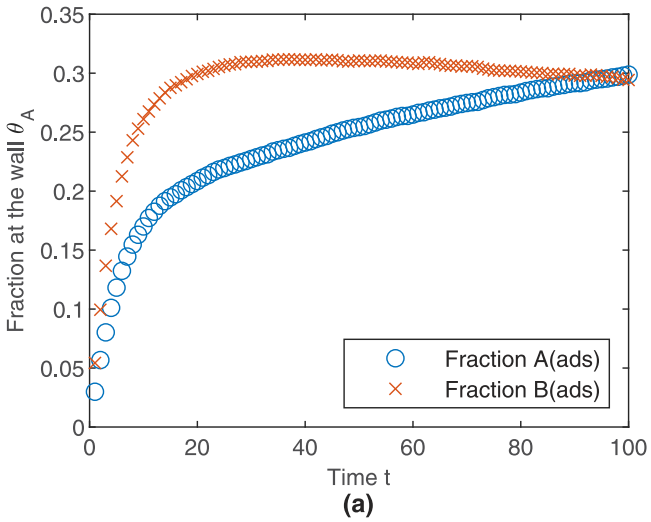

FIG. 8. Non-mean-field elementary reaction mechanism involving a three-step reaction mechanism with reactant dissociation [Eqs. (27)–(29)]. (a) Evolution of the A_{ads} and B_{ads} fraction at the wall for an initial 1:1 A to B_2 molar ratio. (b) Product concentration profile at time $t = 100t_0$ for initial A to B_2 molar ratios of 1:1, 2:1, and 1:2 with no product initially.

The product concentration profile at time $t = 100t_0$ for different initial compositions is compared in Fig. 8(b). This figure shows that at time $t = 100t_0$, there are significant spatial variations in the bulk fluid (especially in the equimolar reactant mixture test case). The total production of C is obtained from the area under these curves. Comparing these areas shows that a 1:1 initial ratio of A to B_2 is preferred as it yields ~25% more production of C than the least optimal composition, being the 2:1 ratio.

Notably, the profiles obtained in Fig. 8(b) are not easily obtainable numerically without making simplifications since the multi-component diffusion models would need to be applied with composition dependent Maxwell–Stefan diffusion coefficients. These then need to be further coupled to the non-linear surface reaction kinetics. This simulation therefore demonstrates the convenience and capability of SRD simulations when having multi-component reactive mixtures with complex reactive boundary conditions.

IV. CONCLUSION

We developed a mesoscopic framework to study heterogeneously catalyzed multi-particle reactions both in the mean-field and non-mean-field regime, connecting mass transport in the fluid to elementary reaction steps on the catalytic surface. Multiple test cases were carried out to demonstrate that the developed method produces the correct reaction behavior. Mean-field elemental reactions can be simulated by neglecting particle–particle interactions on the surface, ensuring that the adsorbed particles can react at any location on the surface. Non-mean-field reactions can be simulated by applying a mesoscopic Monte Carlo simulation on the surface with the bulk fluid simulated by SRD.

Comparing an $A + B \rightarrow C$ reaction in the mean-field and non-mean-field regime demonstrated that the formation of islands for different species can lead to significant coverage differences due to inhibition of reaction rates. These differences demonstrate the importance that surface interactions may have on the total reactivity of a system. Surface mechanisms, such as island formation, are intricately linked to spatial variations in composition, which are in turn related to imposed external forces and flow profiles. Although convective effects were not studied in this work, they can easily be considered.

The method was applied to a heterogeneously catalyzed reaction mechanism in a multi-component gas-phase system with a three-step mechanism involving the initial adsorption of a reactant, its dissociation on the catalyst surface, and a surface reaction. A catalyst poisoning process was simulated by imposing a low desorption rate. This simulation allowed for coupling between detailed surface information (such as surface interaction and coverage results) and spatial concentration variations in the bulk of a multi-component

gas mixture. Allowing for such intricate combinations illustrates the strength of the method developed.

In our future work, we will study how heterogeneous catalytic reaction processes are affected by complex catalyst geometries and geometrical changes caused by chemical reactions such as physical catalyst poisoning. The method can be expanded to non-isothermal systems, providing a new tool to study elementary reactions, which are sensitive to temperature and energy change. After verification with experimental results, the method can serve as a promising candidate for simulating complex reactive processes in heterogeneous catalytic reactors.

ACKNOWLEDGMENTS

R. Fan acknowledges the China Scholarship Council (Grant No. CSC201707720026) for financial support of this work.

AUTHOR DECLARATIONS

Conflict of Interest

The authors have no conflicts of interest to disclose.

DATA AVAILABILITY

The data that support the findings of this study are available from the corresponding author upon reasonable request.

APPENDIX A: NUMERICAL SOLUTION FOR FIRST-ORDER REACTION $A \rightarrow B$

In this work, when validating the simulation with continuum numerical models, the unsteady diffusion partial differential equation (15) valid inside the fluid is discretized along the y axis using a finite difference scheme,

$$C_{A,i}^{l+1} = C_{A,i}^{l} + \frac{D_A \Delta t}{\Delta y^2}(C_{A,i+1}^{l} - 2C_{A,i}^{l} + C_{A,i-1}^{l}). \tag{A1}$$

In this expression, $C_{A,i}^{l}$ represents the particle concentration of species A on an interior cell i at time step l. A similar scheme can be built for the cells at the edge of the nonreactive wall at which a zero flux boundary condition is imposed. If n denotes the cell at this nonreactive boundary, the cell at $n+1$ is fictitious and only used to satisfy the no-flux boundary condition,

$$\left.\frac{dC_A}{dy}\right|_{y=L_y} = 0 \approx \frac{C_{A,n+1}^{l} - C_{A,n-1}^{l}}{2\Delta y}, \qquad C_{A,n+1}^{l} = C_{A,n-1}^{l}. \tag{A2}$$

On the reactive wall, the boundary condition takes the form of

$$-D_A \left.\frac{dC_A}{dy}\right|_{y=0} = -k_{ads}\frac{N_{cat}}{A_{cat}}\theta_v C_A + k_{des}\frac{N_{cat}}{A_{cat}}\theta_A. \tag{A3}$$

In the expression mentioned above, N_{cat} is the total number of catalytic sites while A_{cat} is the total area of the reactive catalyst. The total number of catalyst sites remains constant throughout the simulation. C_A refers to the A concentration at $y = 0$. The boundary cell at the reactive wall can be updated using F_A to represent the flux at the right-hand side of Eq. (A3),

$$-D_A \frac{C_{A,1}^{l} - C_{A,-1}^{l}}{2\Delta y} = F_A \tag{A4}$$

leading to

$$C_{A,-1}^{l} = \frac{2\Delta y F_A}{D_A} + C_{A,1}^{l}, \tag{A5}$$

$$C_{A,0}^{l+1} = C_{A,0}^{l} + \frac{D_A \Delta t}{\Delta y^2}\left(2C_{A,1}^{l} - 2C_{A,0}^{l} + \frac{2\Delta y F_A}{D}\right). \tag{A6}$$

Note that for the derivation of the expression for k_{ads} in Sec. II B, a constant concentration profile was assumed in the bulk. If the difference of concentration between the surface and bulk is small, the SRD and numerical model match very well. Large concentration gradients will require a more elaborate expression for the mean-field adsorption rate constant, which is beyond the scope of this work.

APPENDIX B: ERROR ESTIMATION

Using the Taylor series expansion, the maximum error (Er) associated with Eq. (19) can be calculated as

$$Er = \frac{1}{\rho_{S,A}} \max\left(\frac{\Delta t_s^2}{2}\frac{d^2\rho_A}{dt^2}\right). \tag{B1}$$

Using Eqs. (16) and (17), the second derivative of $\rho_{S,A}$ is calculated as

$$\begin{aligned}\frac{d^2\rho_A}{dt^2} &= -k_{r,AB}\rho_{A_{i-1}}\frac{d\rho_B}{dt} - k_{r,AB}\frac{d\rho_A}{dt}\rho_{B_{i-1}} \\ &= k_{r,AB}^2\rho_{A_{i-1}}^2\rho_{B_{i-1}} + k_{r,AB}^2\rho_{A_{i-1}}\rho_{B_{i-1}}^2.\end{aligned} \tag{B2}$$

Therefore,

$$Er = \frac{\Delta t_s^2}{2}(k_{r,AB}^2\rho_{B_{i-1}}^2 + k_{r,AB}^2\rho_{A_{i-1}}\rho_{B_{i-1}}). \tag{B3}$$

To keep the accuracy of Eq. (21) as high as possible, we aim to keep the relative error of $\frac{\rho_{S,A}}{\rho_{S,A_{i-1}}}$ to stay below 1%. The maximum numerical relative error can be guaranteed to be lower than the following expression:

$$\text{MaxErr} < \frac{1}{2}(P_{re,AB}^2\theta_{B0}^2 + P_{re,AB}^2\theta_{A0}\theta_{B0}). \tag{B4}$$

The surface coverages θ_{B0} and θ_{A0} are bounded between 0 and 1. When the desired maximum relative error is 1%, the condition $P_{re,AB} < 0.14$ is deemed sufficient.

REFERENCES

[1] I. Fechete, Y. Wang, and J. C. Védrine, Catal. Today **189**, 2 (2012).
[2] G. F. Froment, K. B. Bischoff, and J. De Wilde, *Chemical Reactor Analysis and Design* (Wiley, New York, 1990), Vol. 2.
[3] C.-K. Lee and S.-L. Lee, Surf. Sci. **339**, 171 (1995).

[4]K. Malek and M.-O. Coppens, J. Chem. Phys. **119**, 2801 (2003).
[5]N. G. Deen, E. A. J. F. Peters, J. T. Padding, and J. A. M. Kuipers, Chem. Eng. Sci. **116**, 710 (2014).
[6]S. Das, N. G. Deen, and J. A. M. Kuipers, Chem. Eng. Sci. **160**, 1 (2017).
[7]A. Singhal, S. Cloete, S. Radl, R. Quinta-Ferreira, and S. Amini, Chem. Eng. Sci. **172**, 1 (2017).
[8]S. Zhang, X. Zhao, and Z. Yang, Nucl. Sci. Eng. **189**, 135 (2018).
[9]J. Hartig, H. C. Howard, T. J. Stelmach, and A. W. Weimer, Powder Technol. **386**, 209 (2021).
[10]K. Tong, L. Yang, and X. Du, Chem. Eng. J. **400**, 125988 (2020).
[11]X. Ku, T. Li, and T. Løvås, Chem. Eng. Sci. **122**, 270 (2015).
[12]L. Zhang and N. A. Seaton, Chem. Eng. Sci. **49**, 41 (1994).
[13]P. J. Donaubauer, L. Schmalhorst, and O. Hinrichsen, Chem. Eng. Sci. **208**, 115137 (2019).
[14]P. Levitz, J. Phys. Chem. **97**, 3813 (1993).
[15]S. Gimelshein and I. Wysong, Phys. Fluids **29**, 067106 (2017).
[16]S. Swapnasrita, G. R. Pesch, J. A. H. Dreyer, N. Riefler, T. Wriedt, and L. Mädler, Comput.Fluids **187**, 1 (2019).
[17]R. S. Voronov, S. B. VanGordon, V. I. Sikavitsas, and D. V. Papavassiliou, Int. J. Numer. Methods Fluids **67**, 501 (2011).
[18]M. Wang and W. Zhu, Int. J. Heat Mass Transfer **126**, 1222 (2018).
[19]X. Meng and Z. Guo, Phys. Rev. E **94**, 053307 (2016).
[20]C. S. Bresolin and A. A. M. Oliveira, Comput. Phys. Commun. **183**, 2542 (2012).
[21]N. Filipovic, M. Kojic, and A. Tsuda, Philos. Trans. R. Soc., A **366**, 3265 (2008).
[22]Q. Zhu, T. R. Scott, and D. R. Tree, Soft Matter **17**, 24 (2021).
[23]G. Gompper, T. Ihle, D. Kroll, and R. Winkler, *Advanced Computer Simulation Approaches for Soft Matter Sciences III* (Springer, 2009), p. 1.
[24]K. Tucci and R. Kapral, J. Phys. Chem. B **109**, 21300 (2005).
[25]K. Rohlf, S. Fraser, and R. Kapral, Comput. Phys. Commun. **179**, 132 (2008).
[26]A. Sayyidmousavi and K. Rohlf, Phys. Biol. **15**, 046007 (2018).
[27]J.-X. Chen, Y.-G. Chen, and R. Kapral, Adv. Sci. **5**, 1800028 (2018).
[28]P. de Buyl and R. Kapral, Nanoscale **5**, 1337 (2013).
[29]J.-X. Chen and R. Kapral, J. Chem. Phys. **134**, 044503 (2011).
[30]G. Rückner and R. Kapral, Phys. Rev. Lett. **98**, 150603 (2007).
[31]P. de Buyl, Phys. Rev. E **100**, 022603 (2019).
[32]S. Y. Reigh, M.-J. Huang, H. Löwen, E. Lauga, and R. Kapral, Soft Matter **16**, 1236 (2020).
[33]A. Zöttl, Chin. Phys. B **29**, 074701 (2020).
[34]A. Sengar, J. Kuipers, R. A. Van Santen, and J. Padding, Phys. Rev. E **96**, 022115 (2017).
[35]A. Sengar, J. A. M. Kuipers, R. A. van Santen, and J. T. Padding, Chem. Eng. Sci. **198**, 184 (2019).
[36]S. Muehlbauer, S. Strobl, M. Coleman, and T. Poeschel, arXiv:2010.03904 (2020).
[37]W. L. Huang and J. Li, Chem. Eng. Sci. **147**, 83 (2016).
[38]J. Cortés, H. Puschmann, and E. Valencia, J. Chem. Phys. **109**, 6086 (1998).
[39]A. Malevanets and R. Kapral, J. Chem. Phys. **110**, 8605 (1999).
[40]C.-C. Huang, G. Gompper, and R. G. Winkler, Phys. Rev. E **86**, 056711 (2012).
[41]A. Varghese, C.-C. Huang, R. G. Winkler, and G. Gompper, Phys. Rev. E **92**, 053002 (2015).
[42]T. Ihle and D. Kroll, Phys. Rev. E **63**, 020201 (2001).
[43]D. S. Bolintineanu, J. B. Lechman, S. J. Plimpton, and G. S. Grest, Phys. Rev. E **86**, 066703 (2012).
[44]R. Fan, G. T. Zachariah, J. T. Padding, and R. Hartkamp, Phys. Rev. E **104**, 034124 (2021).
[45]T. Ihle, E. Tüzel, and D. M. Kroll, Phys. Rev. E **72**, 046707 (2005).
[46]E. Tüzel, M. Strauss, T. Ihle, and D. M. Kroll, Phys. Rev. E **68**, 036701 (2003).
[47]E. Tüzel, T. Ihle, and D. M. Kroll, Phys. Rev. E **74**, 056702 (2006).
[48]A. Malevanets and R. Kapral, J. Chem. Phys. **112**, 7260 (2000).
[49]M. Ripoll, K. Mussawisade, R. Winkler, and G. Gompper, Phys. Rev. E **72**, 016701 (2005).
[50]W. G. Hoover, Phys. Rev. A **31**, 1695 (1985).
[51]M. Andersen, C. Panosetti, and K. Reuter, Front. Chem. **7**, 202 (2019).
[52]R. LeSar, *Introduction to Computational Materials Science: Fundamentals to Applications* (Cambridge University Press, 2013).
[53]H. Steininger, S. Lehwald, and H. Ibach, Surf. Sci. **123**, 1 (1982).
[54]T. Zambelli, J. V. Barth, J. Wintterlin, and G. Ertl, Nature **390**, 495 (1997).
[55]B. K. Min, A. R. Alemozafar, M. M. Biener, J. Biener, and C. M. Friend, Top. Catal. **36**, 77 (2005).
[56]X. Deng, B. K. Min, A. Guloy, and C. M. Friend, J. Am. Chem. Soc. **127**, 9267 (2005).
[57]G. Veser, F. Esch, and R. Imbihl, Catal. Lett. **13**, 371 (1992).
[58]V. P. Zhdanov and B. Kasemo, Appl. Catal., A **187**, 61 (1999).
[59]P. T. Fanson, W. N. Delgass, and J. Lauterbach, J. Catal. **204**, 35 (2001).
[60]R. Imbihl and G. Ertl, Chem. Rev. **95**, 697 (1995).
[61]A. L. Vishnevskii and V. I. Savchenko, React. Kinet. Catal. Lett. **38**, 167 (1989).
[62]V. I. Elokhin, A. V. Matveev, E. V. Kovalyov, and V. V. Gorodetskii, Chem. Eng. J. **154**, 94 (2009).
[63]N. V. Petrova and I. N. Yakovkin, Surf. Sci. **578**, 162 (2005).
[64]D.-J. Liu and J. W. Evans, Surf. Sci. **603**, 1706 (2009).